HHS Public Access

Author manuscript

Biomaterials. Author manuscript; available in PMC 2017 October 17.

Published in final edited form as:

Biomaterials. 2016 October ; 104: 361–371. doi:10.1016/j.biomaterials.2016.07.029.

In Vivo Targeting of Metastatic Breast Cancer via Tumor Vasculature-Specific Nano-Graphene Oxide

Dongzhi Yang[1,2], **Liangzhu Feng**[3], **Casey A. Dougherty**[1], **Kathryn E. Luker**[1,5], **Daiqin Chen**[1], **Meagan A. Cauble**[4], **Mark M. Banaszak Holl**[4], **Gary D. Luker**[1,5], **Brian D. Ross**[1,5], **Zhuang Liu**[3], and **Hao Hong**[1,5]

[1]Center for Molecular Imaging, Department of Radiology, University of Michigan – Ann Arbor, Michigan 48109-2200, United States

[2]Jiangsu Key Laboratory of New Drug Research and Clinical Pharmacy, Xuzhou Medical University, Xuzhou, Jiangsu 221004, China

[3]Jiangsu Key Laboratory for Carbon-Based Functional Materials and Devices, Institute of Functional Nano and Soft Materials Laboratory (FUNSOM), Soochow University, Suzhou, Jiangsu, China

[4]Department of Chemistry, University of Michigan – Ann Arbor, Michigan 48109-1055, United States

[5]University of Michigan Comprehensive Cancer Center, Michigan 48109-0944, United States

Abstract

Angiogenesis, i.e. the formation of neovasculatures, is a critical process during cancer initiation, progression, and metastasis. Targeting of angiogenic markers on the tumor vasculature can result in more efficient delivery of nanomaterials into tumor since no extravasation is required. Herein we demonstrated efficient targeting of breast cancer metastasis in an experimental murine model with nano-graphene oxide (GO), which was conjugated to a monoclonal antibody (mAb) against follicle-stimulating hormone receptor (FSHR). FSHR has been confirmed to be a highly selective tumor vasculature marker, which is abundant in both primary and metastatic tumors. These functionalized GO nano-conjugates had diameters of ~ 120 nm based on atomic force microscopy (AFM), TEM, and dynamic laser scattering (DLS) measurement. ^{64}Cu was incorporated as a radiolabel which enabled the visualization of these GO conjugates by positron emission tomography (PET) imaging. Breast cancer lung metastasis model was established by intravenous injection of click beetle green luciferase-transfected MDA-MB-231 (denoted as cbgLuc-MDA-MB-231) breast cancer cells into female nude mice and the tumor growth was monitored by bioluminescence imaging (BLI). Systematic *in vitro* and *in vivo* studies have been performed to investigate the stability, targeting efficacy and specificity, and tissue distribution of GO conjugates. Flow cytometry and fluorescence microscopy examination confirmed the targeting specificity of FSHR-mAb attached GO conjugates against cellular FSHR. More potent and persistent uptake of ^{64}Cu-NOTA-GO-FSHR-mAb in cbgLuc-MDA-MB-231 nodules inside the lung was witnessed

*(Z.L.) Fax: 86-512-65882846; Tel: 86-512-65882036; zliu@suda.edu.cn. (H.H.) Fax: 1-734-763-5447; Tel: 1-734-615-4634; hahong@med.umich.edu.

when compared with that of non-targeted GO conjugates (^{64}Cu-NOTA-GO). Histology evaluation also confirmed the vasculature accumulation of GO-FSHR-mAb conjugates in tumor at early time points while they were non-specifically captured in liver and spleen. In addition, these GO conjugates can serve as good drug carriers with satisfactory drug loading capacity (e.g. for doxorubicin [DOX], 756 mg/g). Enhanced drug delivery efficiency in cbgLuc-MDA-MB-231 metastatic sites was demonstrated in DOX-loaded GO-FSHR-mAb by fluorescence imaging. This FSHR-targeted, GO-based nanoplatform can serve as a useful tool for early metastasis detection and targeted delivery of therapeutics.

Graphical Abstract

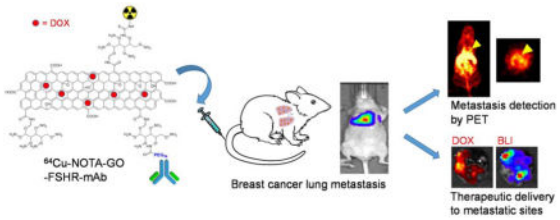

Keywords

Nano-graphene oxide (GO); Angiogenesis; Follicle-stimulating hormone receptor (FSHR); Breast cancer metastasis; Positron emission tomography (PET); Image-guided drug delivery

Introduction

Graphene is a two-dimensional material packed with single-layered carbon atoms. Due to the unique physical, chemical, and mechanical properties, nano-sized graphene and relevant derivatives have attracted tremendous interest for utilization in various biomedical applications [1, 2]. As one important graphene derivative, graphene oxide (GO) with good near-infrared (NIR) absorbance, large specific surface area, good cargo-loading capacity, and versatile reaction capacity, has been frequently utilized as biosensors, drug and gene delivery vectors, imaging contrast agents, and photothermal therapy mediators [3–6]. However, potential adverse effects from GO are limiting factors for its *in vivo* applications. For example, naked GO has been reported to increase intracellular reactive oxygen species (ROS) and trigger mitochondria related apoptosis [7]. Thus, proper functionalization with different macromolecules (e.g. polymers [8, 9], serum protein [10], or polysaccharide [11]) can bestow GO better biocompatibility and mitigated cytotoxicity. It has been demonstrated that GO nanomaterials did not exhibit any noticeable toxicity after modification by polyethylene glycol (PEG) [12]. In this study, branched PEG functionalized nano-sized GO is used as a hybrid platform for both imaging and targeted drug delivery into metastatic breast cancer (MBC).

It is well accepted that angiogenesis is critical for various biological processes including tissue growth, development, and remodeling [13]. As an early event in tumor progression, tumor angiogenesis occurs when the tumor reaches a certain size (usually 1–2 mm in

diameter), as tumors require sustained supply of nutrients and oxygen as well as they need efficient evacuation routes for metabolic wastes [14]. Targeting of angiogenic markers on tumor vasculature has been accepted as a generally applicable strategy for various nanomaterials regardless of tumor types [15]. Among all the identified angiogenic targets, we choose follicle-stimulating hormone receptor (FSHR), a G-protein coupled transmembrane receptor, as our target of interest in this study. The expression of FSHR has been shown to be abundant and confined within the vasculatures of primary tumors [16] and metastatic sites [17] among a variety of cancer types, while it is relatively limited in healthy, quiescent tissues [16, 18–20]. In normal organs/tissues, FSHR is only detectable in ovary and testicular endothelium, osteoclasts, and monocytes [21]. The expression specificity of FSHR can result in superior contrast for cancer detection and makes it an ideal candidate for image-guided drug delivery via nanomaterials.

Despite the abovementioned benefits, utilization of FSHR for cancer detection is currently at a relatively preliminary stage. Positron emission tomography (PET) imaging of prostate tumors by FSHR targeting was initially attempted by using ^{18}F-labeled FSH β 33–53, a FSH fragment [22]. Although decent tumor uptake was shown, fast washout of the tracer from the tumors and a short half-life of ^{18}F (118 min) limited its application in the longitudinal tumor detection. Same research group made an extra effort in a follow-up study to optimize its *in vivo* kinetics by incorporation of a hydrophilic linker [23], however the overall tumor imaging capacity did not get improved. Compared with other ligands, antibodies usually possess stronger and more selective target recognition and thus we chose to use ^{64}Cu-labeled monoclonal antibody (mAb) for PET imaging of FSHR in different cancer types [24]. We confirmed the value of FSHR as a universal tumor detection marker since potent, persistent, and FSHR-correlated tumor uptake of ^{64}Cu-labeled FSHR-mAb was observed in different tumor types (e.g. prostate, breast, and ovarian) [24].

There are also a few research reports on using FSHR for directing nanomaterials to cancer cells or cancerous tissues, especially for ovarian cancer. For example, FSH fragments-conjugated polymer [25] or dendrimer [26] based nanomaterials have been confirmed to selectively bind with FSHR-positive ovarian cancer cells for enhanced drug delivery (e.g. paclitaxel). More recently, paclitaxel-loaded, FSHR-targeted polymer nanoparticles revealed satisfactory *in vivo* treatment efficacy for ovarian cancer lymphatic metastasis [27]. Inspired by those results, here we hope to develop an improved FSHR-targeted nanoplatform for simultaneous tumor detection and therapeutic delivery, and this nanoplatform can be broadly applicable for various tumor types. Since metastases account for over 90% of cancer deaths [28], this nanoplatform should be expected to also accumulate preferably in the metastatic tumor sites.

Breast cancer lung metastasis model is selected due to the large population of breast cancer patients and metastases at distant sites (mainly to the lung, liver and bone) are the main cause of death [29]. In this study, MDA-MB-231 cells were transfected with click beetle green luciferase (cbgLuc) to enable bioluminescence imaging (BLI) of the tumor growth in the lungs. A monoclonal antibody against FSHR (FSHR-mAb) was used as a FSHR-targeting ligand on the PEG-functionalized GO nanosheet. ^{64}Cu was used as a radiolabel to visualize the *in vivo* distribution of GO conjugates via PET imaging. Various *in vitro*, *in*

vivo, and *ex vivo* experiments were carried out to demonstrate FSHR specificity of FSHR-mAb conjugated GO. Ample drug loading (doxorubicin was used as a model drug) and selective drug delivery into metastatic sites were also revealed.

Experimental Section

Chemicals and Reagents

AlexaFluor488-labeled rabbit anti-mouse secondary antibodies were purchased from Lampire biological laboratories (Pipersville, PA). *p*-SCN-Bn-NOTA (*i.e.*, 2-S-(4-isothiocyanatobenzyl)-1,4,7-triazacyclononane-1,4,7-triacetic acid) was purchased from Macrocyclics, Inc. (Dallas, TX). D-luciferin was acquired from Gold Bio Technology (St Louis, MO). $^{64}CuCl_2$ was acquired from the University of Wisconsin cyclotron group. SCM-PEG-Mal (*i.e.* succinimidyl carboxymethyl PEG maleimide, MW: 5 kDa) was purchased from Creative PEG works. FSHR-mAb (catalog number: MAB65591) was purchased from R&D systems (Minneapolis, MN). Chelex 100 resin (50–100 mesh) was acquired from Sigma-Aldrich (St. Louis, MO) and PD-10 size exclusion columns were acquired from GE Healthcare (Piscataway, NJ). Fluorescein isothiocyanate (FITC), Traut's Reagent, TCEP (*i.e.* tris(2-carboxyethyl)phosphine), and all the other reagents were purchased from Fisher Thermo Scientific. All the reagents were directly used without further purifications following manufacturer's instructions. All buffers were prepared from Millipore-grade water and pretreated with the Chelex 100 resin to ensure that the aqueous solution was free of heavy metals.

Synthesis of GO Conjugates

GO-PEG-NH_2 was synthesized according to previously published process [9], which had around 30 amines per GO nanosheets for further functionalization [9]. The attachment of FSHR-mAb and imaging label (^{64}Cu) onto GO conjugates were conducted according to our previously reported procedures with minor modifications [3]. In brief, FSHR-mAb was mixed with Traut's reagent at a molar ratio of 1:40 at the pH of 8.0 for incorporation of thiols onto the antibody molecule. After 2 h of incubation at room temperature (RT), the resulting FSHR-mAb-SH was purified by PD-10 column using Chelex-100 treated phosphate-buffered saline (PBS) as the mobile phase. Based on titration results from Ellman's reagent, we calculated that there were 5 thiol groups per FSHR-mAb on average under this reaction condition.

GO-PEG-NH_2 was mixed with p-SCN-Bn-NOTA or FITC at a molar ratio of 1:10 at pH 9.0 for 1 h. The resulting NOTA-GO (or fluorescein-GO) was subsequently reacted with SCM-PEG-Mal at pH 8.5 at a molar ratio of 1:30 for 2 h. After purifying by centrifugation filtration using 50 kDa cut off Amicon filters, the resulting reaction intermediates (NOTA-GO-PEG-Mal or fluorescein-GO-PEG-Mal) were obtained. Subsequently, NOTA-GO-PEG-Mal, or fluorescein-GO-PEG-Mal was mixed with FSHR-mAb-SH at a molar ratio of 1:5 at the pH of 7.5 in the presence of TCEP to protect thiols from oxydation. After reacting overnight at 4°C, the final products termed NOTA-GO- FSHR-mAb and fluorescein-GO-FSHR-mAb (PEG was omitted for clarity purpose) were collected after PD-10 purification in order to remove the excessive TCEP.

Material characterization

The morphology of GO conjugates was evaluated by JEM-1400Plus transmission electron microscope (JEOL USA, Peabody, MA) and Bruker Dimension ICON atomic force microscope (Bruker, Billerica, MA). Meanwhile, their hydrodynamic size and size distribution, as well as ζ-potentials were determined by dynamic light scattering (DLS) (ZetaSizer Nano ZS90, Malvern Instrument, USA), at the concentration of 0.05 mg/ml (based on GO).

Drug loading/releasing measurement

Doxorubicin (DOX) was used as a model drug to test the drug loading capacity of these GO conjugates. NOTA-GO-FSHR-mAb (~1.82 mg/mL) was mixed with 3.34 mmol/L of DOX at pH 8 overnight. Unbound excess DOX was removed by filtration through a 10 kDa filter with repeated rinsing of PBS. The resulting NOTA-GO(DOX)-FSHR-mAb was re-suspended in PBS and stored at 4 °C. Drug release was evaluated at 37 °C in an acetate buffer (pH 5.3) and a phosphate buffer (pH 7.4). NOTA-GO(DOX)-FSHR-mAb was placed in a dialysis bag with a molecular weight cut-off of 2 kDa. The dialysis bag was immersed in the release medium and kept in a shaker (100 rpm) under RT. Samples of 0.2 ml volume were periodically removed and the same volume of fresh medium was added. The amount of released DOX was analyzed with a spectrophotometer at 485 nm. The drug release studies were performed in triplicate for each sample.

^{64}Cu-labeling and stability evaluation

$^{64}CuCl_2$ (~185 MBq, in 0.1 M hydrochloric acid) was diluted with 0.1 M sodium acetate (pH 6.5) and added to 75 μg of NOTA-GO or NOTA-GO-FSHR-mAb, and the final reaction pH was at the range of 4 – 5.5. The reaction was allowed to proceed for 0.5 – 1 h at 37°C with constant shaking (350 rpm). ^{64}Cu-NOTA-GO or ^{64}Cu-NOTA-GO-FSHR-mAb was purified by a PD-10 column using PBS as the mobile phase.

For serum stability studies, ^{64}Cu-NOTA-GO-FSHR mAb or ^{64}Cu-NOTA-GO was incubated in complete mouse serum at 37°C for up to 24 h (same time period used for serial PET imaging). Portions of the mixture were sampled at different time points and filtered through 100 kDa cutoff filters. The radioactivity of collected filtrates was measured in a WIZARD^2 gamma counter (Perkins-Elmer). The percentages of retained (*i.e.*, intact) ^{64}Cu on the GO conjugates (^{64}Cu-NOTA-GO-FSHR mAb or ^{64}Cu-NOTA-GO) were calculated using the equation [(total radioactivity - radioactivity in filtrate)/total radioactivity ×100%].

Flow Cytometry and Fluorescence Microscopy

FSHR-positive MDA-MB-231 cells [24] and FSHR-negative SKOV-3 cells [24] were harvested and resuspended in cold PBS (supplemented with 2% bovine serum albumin) to a final concentration of 2×10^6 cells/mL. After incubation with fluorescein-GO-FSHR-mAb and fluorescein-GO (5 μg/mL based on GO) for 0.5 h at 37°C, the cells were washed thrice with cold PBS. Afterwards, the cells were resuspended in PBS and analyzed using a BD LSR Fortessa four-color analysis cytometer (Becton-Dickinson, San Jose, CA), equipped with 488 and 633 nm laser. FlowJo (version: X.0.7, Tree Star Inc.) was used to analyze the cellular fluorescence from different treatment groups. Cells were also examined under a

Nikon A1 confocal fluorescence microscope to validate the fluorescence-activated cell sorting (FACS) results.

Cell Culture and Animal Model

MDA-MB-231 cells were purchased from the American type culture collection (ATCC, Manassas, VA). Detail procedures for stable transfection of MDA-MB-231 cells with click beetle green luciferase were similar with a previous report [30]. cbgLuc-MDA-MB-231 cells were maintained in DMEM medium (Invitrogen, Carlsbad, CA) supplemented with 10% fetal bovine serum at 37 °C with 5% CO_2. Cells were used when they reached ~75% confluence.

All animal procedures were performed according to a protocol approved by University of Michigan Committee on Use and Care of Animals (UCUCA, protocol number: PRO00006023). The cbgLuc-MDA-MB-231 breast cancer experimental lung metastasis model was established by intravenous (*i.v.*) injection of 2×10^5 cbgLuc-MDA-MB-231 cells in 100 μL of PBS into 6-week-old female nude mice (Charles River). The bioluminescence imaging (BLI) signal of the mice was monitored regularly using an IVIS Spectrum system (Perkin-Elmer). Mice were used for imaging studies when the BLI signals from the thoracic area of mice were substantially strong (typically 4 weeks after inoculation).

Western Blotting

MDA-MB-231, cbgLuc-MDA-MB-231 and SKOV-3 cells were homogenized in ice-cold RIPA buffer supplemented with protease inhibitors (Complete Protease Inhibitor Cocktail, Roche, Basel, Switzerland) and phosphatase inhibitors (PhosSTOP, Roche, Basel, Switzerland). Concentration of protein was determined using Lowry assays (Bio-Rad, Hercules, CA) and equal amount of whole protein lysate was loaded in each lane and resolved using 4–12% gradient Bis-Tris gel (Invitrogen, CA). Proteins were transferred to 0.2 μm nitrocellulose membrane (Invitrogen, CA). Membrane was incubated overnight at 4 °C with primary antibodies after blocking with 5% milk, followed by incubation with appropriate horseradish peroxidase (HRP)-conjugated secondary antibody at room temperature for one hour. Membrane was incubated with HRP-conjugated anti-β-actin for 1 h at RT after blocking with 5% milk for the internal standard test. ECL-Plus was used to detect the activity of peroxidase according to the manufacturer's protocol (Amersham Pharmacia, Uppsala, Sweden).

PET Imaging and Biodistribution Studies

The mice bearing cbgLuc-MDA-MB-231 tumor nodules in lungs were each injected with 5–10 MBq of ^{64}Cu-labeled GO conjugates via tail vein, and 3–15 min static PET scans were performed. Inveon microPET/microCT rodent scanner (Siemens Medical Solutions USA, Inc.) was used for PET scanning at the chosen time points post-injection (p.i.). All the images were reconstructed through a 3D ordered subset expectation maximization (3D OSEM) algorithm, with no attenuation or scatter correction applied. Using the vendor software (Inveon Research Workplace, Ed 4.2), the three-dimensional region-of-interest (ROIs) were circled over the tumor and major organs on decay-corrected whole-body images [31]. Assuming a tissue density of 1 g/ml, the ROIs were converted to MBq per gram using a

conversion factor, and then divided by the total administered radioactivity to obtain an image ROI-derived percentage injected dose per gram of tissue (%ID/g). After the last PET scan at 24 h *p.i.*, biodistribution studies were conducted to confirm the organs uptake quantified by PET. The mice were euthanized and their blood, lung (with tumor nodules), and major organs/tissues were collected and wet-weighed. The radioactivity in each collected sample was measured using the WIZARD^2 gamma counter (Perkin-Elmer) and presented as %ID/g (means ± SD). The cbgLuc-MDA-MB-231 tumor nodules, liver and spleen were also frozen for histological analysis.

Histology

Tissues were cut into frozen slices of 6 μm thickness. After being fixed with cold acetone for 10 min, the tissues were rinsed with PBS and blocked by 2% BSA for 30 min. Subsequently, the tissue slides were stained for endothelial marker CD31 with a rat anti-mouse CD31 antibody (2 μg/mL) for 1 h, followed by Cy3-labeled donkey anti-rat IgG (2.5 μg/mL) for 2 h. The locations of NOTA-GO-FSHR-mAb conjugates were visualized by using an AlexaFluor488-labeled rabbit anti-mouse IgG (which recognizes the location of FSHR-mAb on GO conjugates). All fluorescence images were taken with a Nikon A1 confocal microscope with a magnitude of 200×.

Results

Preparation and Characterization of GO conjugation

Four derivatives of GO-PEG-NH_2 were prepared and studied in this work: NOTA-GO, NOTA-GO-FSHR-mAb, fluorescein-GO and fluorescein-GO-FSHR-mAb. The schematic structures of these conjugates are shown in Figure 1a. The two derivatives with fluorescein attachment (*i.e.* fluorescein-GO and fluorescein-GO-FSHR-mAb) were primarily employed for *in vitro* evaluation of FSHR targeting specificity using fluorescence techniques, while the two conjugates with NOTA attachment (*i.e.* NOTA-GO and NOTA-GO-FSHR-mAb) were subsequently labeled with ^{64}Cu for *in vivo* PET imaging and biodistribution studies.

The size distribution histogram of these GO conjugates measured by DLS is shown in Figure 1b. The average hydrodynamic diameter of GO-PEG-NH_2 is 68 nm. As expected, the average hydrodynamic diameter NOTA-GO increases to 92 nm post NOTA conjugation and the number further increases to 220 nm for NOTA-GO-FSHR-mAb. The size distribution of these GO conjugates was relatively narrow. At the same time, ζ-potential of GO-PEG-NH_2, NOTA-GO and NOTA-GO-FSHR-mAb is 3.45, 0.39 and 3.99 mV, respectively, which serves as further evidence for successful NOTA/antibody conjugation. Based on the atomic force microscopy (AFM) measurements in Figure 1c, GO-PEG-NH_2 and NOTA-GO-FSHR-mAb were small sheets with the average diameter of 30–50 nm and ~120 nm, respectively. The size difference confirmed the successful conjugation of FSHR-mAb (150 kDa molecular weight), NOTA and PEG on to the surface of GO-PEG-NH_2. The reason that the sizes of GO conjugates measured by AFM were smaller than that measured by DLS was that DLS measures the hydrodynamic diameters with hydrophilic PEG layers extending into the aqueous solution while the AFM measures the diameter of dried GO conjugates. Transmission electron microscopy (TEM) was also taken to confirm the sheet-like

morphology of these GO conjugates (Figure 1d). Simultaneously, SDS-PAGE and protein blot were both used as further evidence that FSHR-mAb was truly attached onto GO conjugates (Figure S1).

In Vitro Investigation of GO Conjugates

To evaluate the FSHR-targeting characteristics of GO conjugates, the flow cytometry analysis and microcopy studies of fluorescein-GO and fluorescein-GO-FSHR-mAb were conducted in MDA-MB-231 cells (FSHR-positive [24]) and SKOV-3 cells (FSHR-negative [24]). Western blot was used to confirm the expression profile in these two cell lines and illustrate that cbgLuc transfection did not alter cellular FSHR level in MDA-MB-231 (Figure 2a). There were more than 10-fold expression difference of FSHR in MDA-MB-231 cells compared with SKOV-3 (based on Western blot), which corroborated with immunological staining results for FSHR in these cells (Figure S2). As can be seen in the FACS data from Figure 2b, incubation with 5 μg/mL of fluorescein-GO-FSHR-mAb greatly enhanced the cellular fluorescence intensity compared with incubation of fluorescein-GO at the same concentration (~8.0 fold higher than the fluorescein-GO group). In comparison, both fluorescein-GO-FSHR-mAb and fluorescein-GO did not show obvious cellular fluorescence enhancement in FSHR-negative SKOV-3 cells. This results were further validated in a confocal fluorescence microscope evaluation (Figure 2c). To further confirm the FSHR specificity of fluorescein-GO-FSHR-mAb, we used sonication (30 min) to denature FSHR-mAb on its surface. Denatured fluorescein-GO-FSHR-mAb gave very low cellular fluorescence signals in MDA-MB-231 cells, which confirmed FSHR-targeting specificity from FSHR-mAb incorporation. Although sonication here could eliminate the FSHR-targeting capacity from fluorescein-GO-FSHR-mAb, it did not seem to affect its structural integrity or cause the detachment of FSHR-mAb from GO (Figure 1b and S1). By taking together the results, we can conclude that FSHR-mAb conjugation and cellular FSHR targeting is one of the controlling factors to mediate cellular internalization of fluorescein-GO-FSHR-mAb into MDA-MB-231. Thus, it provided justification for *in vivo* investigation of NOTA-GO-FSHR-mAb.

The decay-corrected radiochemical yield was 56 ± 7 % (n = 10) for the labeling of ^{64}Cu onto NOTA-GO and NOTA-GO-FSHR-mAb, based on the reaction ratio of 15 μg NOTA-GO or NOTA-GO-FSHR-mAb per 37 MBq of ^{64}Cu, with radiochemical purity of > 95%. The specific activity of both ^{64}Cu-NOTA-GO and ^{64}Cu-NOTA-GO-FSHR-mAb was ~1.38 GBq/mg, assuming complete recovery of ^{64}Cu-NOTA-GO and ^{64}Cu-NOTA-GO-FSHR-mAb after size exclusion column. Since PET imaging detects the radioactive nuclides (in this report ^{64}Cu) rather than the GO conjugates, excellent *in vivo* stability is a prerequisite that the signal acquired from PET imaging truly reflects the distribution profile of the GO conjugates. To confirm this, serum stability evaluation was carried out to ensure that the ^{64}Cu-NOTA-GO and ^{64}Cu-NOTA-GO-FSHR-mAb are sufficiently stable *in vivo*. More than 91% of ^{64}Cu retained on the GO conjugates over a 24 h incubation period (Figure 2d), indicating excellent stability of these ^{64}Cu-labeled GO conjugates. Also, by DLS and zeta-potential measurement, no noticeable changes of these GO conjugates were identified post serum incubation (Figure S6).

BLI to Monitor Lung Metastasis

About two weeks after *i.v.* injection, BLI signal from the cbgLuc-MDA-MB-231 cells in mouse lung area started to become apparently detectable with the BLI signal intensity of 8.9×10^5 photons/sec/cm^2/sr (Figure 3a). At about one month after tumor inoculation, the mice bearing cbgLuc-MDA-MB-231 lung metastasis tumors were used for subsequent PET/fluorescence imaging studies when the BLI signal intensity was sufficiently strong (BLI intensity of 7.4×10^7 photons/sec/cm^2/sr) but before mice showed observable symptoms (e.g., body weight loss, difficulty in breathing, etc.). The diameter of tumor nodules inside the lung was measured post-mortem to be 1.7 ± 0.6 mm (n = 10), which have sufficient angiogenesis level, consistent with our previous findings [32].

In Vivo PET Imaging

Based on our previous experience of in vivo tumor targeting and imaging with radiolabeled nanomaterials [33–36], the time points of 0.5, 2, 4 and 24 h post-injection (*p.i.*) were chosen for serial PET scans to show the in vivo distribution profiles of these ^{64}Cu-labeled GO conjugates. By using dynamic PET scans, the circulation half-life of ^{64}Cu-NOTA-GO-PEG-FSHR-mAb was calculated to be 3.5 ± 1.7 h (n = 3, Figure S3). The coronal and cross-sectional images that contain the cbgLuc-MDA-MB-231 metastatic tumor nodules are shown in Figure 3b and Figure 3c. Potent uptake of ^{64}Cu-NOTA-GO-FSHR-mAb was observed as early as 0.5 h *p.i.* with PET in the small tumor modules inside the lung. At the same time, significant amount of radioactivity could also be found in the liver and abdomen area. Quantitative data obtained from ROI analysis of the PET results are shown in Figure 4.

The accumulation of ^{64}Cu-NOTA-GO-FSHR-mAb in the cbMDA-MB-231 tumor nodules was very fast - clearly visible (10.6 ± 1.1 %ID/g) at 0.5 h *p.i.* and remained relatively stable at all the time points examined (10.6 ± 1.0, 11.6 ± 1.1, 9.3 ± 0.9 %ID/g at 2, 4 and 24 h *p.i.* respectively, n = 4, Figure 4a and Table 1), which provided excellent tumor contrast. Multiple visible tumor nodules in the lung were observable in Figure 3c. When intravenously injected, most nanomaterials were excreted from the animals primarily through the hepatobiliary and/or renal pathway [37]. Since the diameters of GO conjugates investigated in this study are significantly larger than the cutoff for renal filtration (~5 nm), they are cleared primarily through the hepatobiliary pathway. The liver uptake of ^{64}Cu-NOTA-GO-FSHR-mAb was 16.5 ± 4.0, 17.8 ± 1.2, 15.8 ± 2.5 and 15.6 ± 1.9%ID/g at 0.5, 2, 4 and 24 h *p.i.* respectively, while the radioactivity in the blood was 7.2 ± 2.0, 4.6 ± 1.7, 4.5 ± 0.5 and 4.7 ± 1.1%ID/g at 0.5, 2, 4 and 24 h *p.i.* respectively (n = 4, Table 1). From these data, we can find that the clearance of ^{64}Cu-NOTA-GO-FSHR-mAb from blood is much faster than that from tumor nodules, while its excretion is primarily from liver at a relatively slow speed. Combining with the fact that the accumulation of ^{64}Cu-NOTA-GO-FSHR-mAb in normal tissues (e.g. muscle) is very low, it was justifiable for us to conclude that its tumor detection contrast is very high. *In vivo* pharmacokinetics of ^{64}Cu-NOTA-GO-FSHR-mAb were also evaluated in healthy, tumor-free mice (n = 3, without cancer cell injection), which were similar to what was observed in tumor-bearing mice (Figure S4 and Table S1).

Similar to the *in vitro* study, antibody denature was also performed to confirm FSHR targeting specificity of ^{64}Cu-NOTA-GO-FSHR-mAb *in vivo*. Sonication of 30 min before ^{64}Cu-NOTA-GO-FSHR-mAb administration could significantly reduce the tumor uptake at all time points examined ($p< 0.01$, n = 3, Figure 4b and Table 1), which confirmed that conjugation of FSHR-mAb could be the primary contributor for enhanced tumor accumulation of these GO conjugates. Liver uptake of ^{64}Cu-NOTA-GO-FSHR-mAb in the "denatured" group was comparable to ^{64}Cu-NOTA-GO-FSHR-mAb (Table 1). Faster blood clearance at early time points (0.5 h and 2 h) was demonstrated for ^{64}Cu-NOTA-GO-FSHR-mAb with denature, while its circulation retention was similar to that of ^{64}Cu-NOTA-GO-FSHR-mAb at late time points (4 h and 24 h).

In contrast, without the conjugation of FSHR-mAb (*i.e.* passive targeting alone), the tumor uptake of ^{64}Cu-NOTA-GO in cbgLuc-MDA-MB-231 tumor nodules (3.8 ± 0.4, 3.1 ± 0.5, 3.3 ± 0.7,1.9 ± 0.4 %ID/g at 0.5, 2, 4 and 24 h *p.i.*, respectively; n = 3; Figure 4c) was significantly lower than that of ^{64}Cu-NOTA-GO-FSHR-mAb ($p<0.01$) at all time points examined, further demonstrating FSHR specificity of ^{64}Cu-NOTA-GO-FSHR-mAb in vivo. Compared with ^{64}Cu-NOTA-GO-FSHR-mAb, liver uptake of ^{64}Cu-NOTA-GO was similar and the radioactivity of ^{64}Cu-NOTA-GO in blood was also comparable.

Figure 4d summarizes the uptake of these GO conjugates in cbgLuc-MDA-MB-231 tumor nodules over time. The differences between the tumor uptake of ^{64}Cu-NOTA-GO-FSHR-mAb and the two control groups (*i.e.* ^{64}Cu-NOTA-GO and the "denatured" group) were statistically significant ($P <0.01$, n = 3) at all time points examined. Besides significantly improved tumor targeting efficacy, the tumor-to-muscle (T/M) ratios increased as well. As shown in Figure 4e and Table 2, T/M value of the targeted group was 15.1 ± 3.4 at 0.5 h *p.i.*, and peaked at 4 h *p.i.* (19.3 ± 6.4), significantly higher than that of ^{64}Cu-NOTA-GO (5.5 ± 0.3 at 4 h *p.i.*) and denatured groups (4.0 ± 1.6 at 4 h *p.i.*). These T/M ratios confirmed that FSHR-mAb conjugation onto GO could result in very optimal contrast for (metastatic) tumor detection.

Biodistributions

Figure 5 shows the biodistribution data from γ-counting at 24 h *p.i.* to validate the PET results. The organ distribution results obtained from biodistribution studies matched very well with PET ROI quantifcation, confirming that PET imaging accurately reflected the distribution of these ^{64}Cu-labeled GO conjugates. The organ absorption analysis revealed that the uptake of ^{64}Cu-NOTA-GO-FSHR-mAb was similar to the two controls (non-targeting and denatured groups) in most organs except the cbgLuc-MDA-MB-231 tumor-bearing lung. A T/M ratio of 14.6 ± 4.7 was obtained for ^{64}Cu-NOTA-GO-FSHR-mAb at 24 h *p.i.* Some of separable cbgLuc-MDA-MB-231 tumor nodules (n = 5 per group) from the lungs were also chosen for radioactivity measurement, and it was found that the individual uptake of ^{64}Cu-NOTA-GO-FSHR-mAb in these tumor nodules could be even higher than the PET findings and reached 19.7 ± 2.1 %ID/g.

Histology

To further confirm the distribution of GO conjugates in different tissues/organs, histological studies were carried out in this study. Due to the significant uptake of ^{64}Cu-NOTA-GO-FSHR-mAb in liver and spleen, the mice injected with ^{64}Cu-NOTA-GO-FSHR-mAb were euthanized at 24 h *p.i.* after the last PET scans, and then cbgLuc-MDA-MB-231 tumor nodules-containing lungs, liver and spleen were frozen and cryo-sectioned for the immunofluorescence staining. Hematoxylin and eosin (H&E) staining was used in tumor nodules-containing lungs to confirm the existence and location(s) of cbgLuc-MDA-MB-231 tumor nodules (Figure 6). From H&E staining results, abnormally clustered tumor cells and irregular nuclei morphology could be seen in cbgLuc-MDA-MB-231 tumor nodules, while regularly shaped epithelium lining and normal alveoli structure was observed in normal lung tissues. For the immunohistology analysis, FSHR-mAb within the structure of NOTA-GO-FSHR-mAb served as the primary antibody. Thus, the green fluorescence in Figure 6 was attributed to the presence of NOTA-GO-FSHR-mAb in all the examined tissues. As indicated in Figure 6, there were substantial amounts of NOTA-GO-FSHR-mAb accumulated in cbgLuc-MDA-MB-231 tumor, liver and spleen, which was consistent with the PET imaging results.

The specificity of NOTA-GO-FSHR-mAb against cbgLuc-MDA-MB-231 tumors was further established since no existence of NOTA-GO-FSHR-mAb was found in the surrounding normal lung tissues (Figure 6). Partial overlap of green fluorescence from NOTA-GO-FSHR-mAb with the red fluorescence (which delineates CD31, a vasculature marker) in cbgLuc-MDA-MB-231 tumor nodules at 24 h *p.i.* indicated significant extravasation of NOTA-GO-FSHR-mAb from vasculature at that time. Furthermore, NOTA-GO-FSHR-mAb was primarily located on the tumor vasculature with little extravasation at 0.5 h p.i., which proved that vasculature-targeting is truly responsible for the enhanced tumor uptake of these GO conjugates. On the other hand, the green fluorescence (attributed to NOTA-GO-FSHR-mAb) in the liver and spleen exhibited very weak overlay with the vasculatures, suggesting that NOTA-GO-FSHR-mAb did not target regular vasculatures inside these organs. Their uptake was most likely due to non-specific capture by mononuclear phagocyte system (MPS, e.g. macrophages). Taken together, the results from immunofluorescence images corroborated with *in vivo* observations, indicating that NOTA-GO-FSHR-mAb was quite stable *in vivo* and was specifically target FSHR in the tumor vasculature.

Enhanced drug delivery into MBC

We have demonstrated that selective accumulation of GO conjugates in MBC metastasis, and here we provided further evidence that they could become attractive nanocarriers for future drug delivery applications. A good drug loading capacity of 756 mg/g was achieved. Since DOX is known to be intrinsically pH sensitive, a pH-sensitive DOX release profile was also observed in NOTA-GO(DOX)-FSHR-mAb, where a faster DOX release rate (69.3% drug release at 48 h) was shown at acidic condition (pH 5.0) compared with that at neutral condition (24.2% drug release at 48 h, pH 7.4, Figure S5). No significant size change was found for NOTA-GO-FSHR-mAb post loading of DOX (Figure 1b and S6).

As a proof-of-concept, we further demonstrated the feasibility of enhanced tumor targeted drug delivery *in vivo* using FSHR-mAb conjugated NOTA-GO(DOX), denoted as NOTA-GO(DOX)-FSHR-mAb. cbgLuc-MDA-MB-231 lung nodules-bearing mice were injected with NOTA-GO(DOX)-FSHR-mAb and NOTA-GO(DOX) (1.1 mg GO/kg, 0.84 mg DOX/kg for both groups). The mice were then sacrificed at 0.5 h p.i, and the major organs were collected and imaged in the IVIS Spectrum system (Ex=465 nm, Em=580 nm) to detect the tissue presence of DOX (Figure 7). It is important to note that due to different absorption/scattering behaviors of DOX in various tissues, optical signal intensities from different organs may not accurately reflect the absolute uptake level of injected NOTA-GO(DOX) conjugates. For example, although liver is the dominant accumulation organ for GO conjugates, only weak optical signal could be observed based on *ex vivo* fluorescence imaging because of its dark color and strong absorbance of visible DOX fluorescence (Figure 7). In contrast, due to the much lighter color of tumor nodules-containing lungs, intense fluorescence signal from DOX could be observed in mice injected with NOTA-GO(DOX)-FSHR-mAb, which is significantly stronger than the control group without FSHR-mAb conjugation. Moreover, the distribution pattern of DOX correlated sufficiently well with the location of tumor nodules from BLI observation. Therefore, the significantly enhanced tumor targeting efficiency and optimal drug loading capacity will make antibody conjugated GO conjugates highly attractive for image-guided therapeutic delivery into MBC.

DISCUSSIONS

Graphene derivatives are attractive carriers for loading of different cargos including anticancer drugs, since they possess ultra-high surface area, strong **π-π** interaction, and versatile reaction capacity with a variety of substance. Moreover, graphene derivatives can absorb NIR laser and transfer the energy into heat, which can be used for more controllable (heat triggered) drug release [9]. The oxidation of graphene into GO often serves as the primary precursor for further functionalization with different bioactive molecules and enables their usage in a variety of biomedical applications [38]. In this study, GO nanosheets were initially functionalized with branched PEG before they were attached to NOTA (for ^{64}Cu labeling) and FSHR-mAb. Potent and persistent uptake of ^{64}Cu-NOTA-GO-FSHR-mAb into cbgLuc-MDA-MB-231 tumor nodules in the lungs is the strong evidence that these GO conjugates are extremely useful for (metastatic) tumor detection. We understand that the lung metastasis tumor model used in this study may be considered as more “artificial” but it is sufficient for proof-of-principle purposes. Detailed investigation of these GO conjugates on more clinically relevant cancer models (e.g. spontaneous metastasis [39] or patient-derived xenografts [40]) will be carried out separately in the future. Although the physical properties (e.g. photothermal transition) of GO conjugates are not utilized, also the therapeutic effect of NOTA-GO(DOX)-FSHR-mAb was not evaluated in the current study, it may serve as a founding piece for future theranostic application of MBC involving GO conjugates.

For *in vivo* tumor targeting using nanomaterials including GO, vasculature targeting is a promising approach since extravasation of many nanomaterials can prove to be difficult [41]. Recently, FSHR is identified as a universal tumor angiogenesis target, and this receptor has

already been used for ovarian cancer targeting both *in vitro* and *in vivo* [26, 27]. However, traditional peptide [42, 43] or polypeptide [27] based FSHR ligands usually have unsatisfactory stability and target-binding affinity *in vivo*. In comparison, FSHR antibody exhibited higher affinity, better resistance to degradation, and simpler conjugation chemistry. The high specificity in tumor, and the limited accumulation in other normal tissues from this work clearly suggest that FSHR-mAb is good directing agent for GO conjugates to accumulate in tumor vasculature for imaging or therapeutic delivery purposes.

Similar to many other nanomaterials, uptake of GO conjugates in mononuclear phagocyte system (MPS, such as liver and spleen) is inevitably high. One possible reason may be due to the attachment of FSHR-mAb, which possesses long circulation time in blood and interacts actively with circulating immune cells. To improve the in vivo pharmacokinetics, attachment of engineered antibody fragments (e.g. Fab, $F(ab')_2$, diabody, nanobody etc.) can potentially decrease non-specific binding, increase tumor penetration, and possess more adjustable circulation time [44–46], which is one of our research focus in the future.

The good tumor retention and optimal tumor-to-background ratio encouraged us to load DOX as a model drug and test its delivery efficiency into the (metastatic) tumor sites. Judging from *ex vivo* fluorescence imaging results, more potent delivery efficacy was witnessed for DOX-loaded GO conjugates when they were coupled with FSHR-mAb. In our current study, we cannot discriminate whether the tumor fluorescence is from NOTA-GO(DOX)-FSHR-mAb or from free DOX detached from GO conjugates, but a more important conclusion is that DOX delivery into cbgLuc-MDA-MB-231 tumor nodules is truly enhanced by GO conjugates. In addition, using one drug for cancer therapy is usually considered as ineffective: tackling on a specific target pathway often result in the activation of more pathogenic pathways as a compensation [47, 48]. Therefore, combinatorial therapies using multiple therapeutic agents together for generating synergistic effects is a logical approach to combat cancer since they can respond to the dynamic nature of cancer during the treatment. Different combinations of drugs/genes/therapeutic isotopes (e.g. ^{67}Cu) can be loaded onto GO conjugates designed in this study for the future therapy. For example, the combination loading of anti-angiogenic (e.g. sunitinib) and anti-proliferation (e.g. MEK inhibitor trametinib) drugs are under test from us for synergistic therapeutic effects.

The future of nanomedicine lies in multifunctional nanoplatforms that have both therapeutic components and imaging labels. Other inorganic nanomaterials, such as magnetic iron oxide (IONPs) and silica-based nanoparticles [49], can be grown on the surface of GO, obtaining hybrid graphene nanomaterials for multimodal imaging. At the same time, graphene-based nanomaterials are usually considered as “low degradable” *in vivo*, thus complexing with other materials/molecules is one strategy to tune their pharmacokinetics in the test subjects [50]. With further optimization, these GO conjugates can be used as a “smart” player for imaging-guided cancer therapy.

Conclusions

In this study, we demonstrated efficient (metastatic) tumor targeting of GO conjugates in an experimental murine model of breast cancer lung metastasis, in which FSHR was used as the

target-of-interest. FSHR is ubiquitously expressed in the vasculatures from a wide variety of cancer types, making it suitable for nanomaterial-based tumor targeting. Based on various in vivo/in vitro/ex vivo studies, the GO conjugates exhibited excellent stability and high specificity for FSHR. Serial PET imaging revealed rapid tumor uptake of ^{64}Cu-NOTA-GO-FSHR-mAb and remained stable over time. Importantly, NOTA-GO-FSHR-mAb can also serve as a highly efficient drug delivery vector into metastatic breast cancer.

Supplementary Material

Refer to Web version on PubMed Central for supplementary material.

Acknowledgments

This work is supported, in part, by the University of Michigan Department of Radiology (startup to H. H.), Else U. Pardee Foundation, the National Basic Research Program (973 Program) of China (2012CB932600, 2011CB911002), the National Natural Science Foundation of China (51132006, 51002100, 81201696), and Jiangsu Government Scholarship for Overseas Studies.

References

1. Syama S, Mohanan PV. Safety and biocompatibility of graphene: A new generation nanomaterial for biomedical application. Int J Biol Macromol. 2016; 86:546–55. [PubMed: 26851208]
2. Zhou X, Liang F. Application of graphene/graphene oxide in biomedicine and biotechnology. Curr Med Chem. 2014; 21:855–69. [PubMed: 24251572]
3. Hong H, Yang K, Zhang Y, Engle JW, Feng L, Yang Y, Nayak TR, Goel S, Bean J, Theuer CP. In vivo targeting and imaging of tumor vasculature with radiolabeled, antibody-conjugated nanographene. ACS Nano. 2012; 6:2361–70. [PubMed: 22339280]
4. Chen J, Badioli M, Alonso-González P, Thongrattanasiri S, Huth F, Osmond J, Spasenović M, Centeno A, Pesquera A, Godignon P. Optical nano-imaging of gate-tunable graphene plasmons. Nature. 2012; 487:77–81. [PubMed: 22722861]
5. Hong H, Zhang Y, Engle JW, Nayak TR, Theuer CP, Nickles RJ, Barnhart TE, Cai W. In vivo targeting and positron emission tomography imaging of tumor vasculature with ^{66}Ga-labeled nano-graphene. Biomaterials. 2012; 33:4147–56. [PubMed: 22386918]
6. Rong P, Yang K, Srivastan A, Kiesewetter DO, Yue X, Wang F, Nie L, Bhirde A, Wang Z, Liu Z. Photosensitizer loaded nano-graphene for multimodality imaging guided tumor photodynamic therapy. Theranostics. 2014; 4:229–39. [PubMed: 24505232]
7. Li Y, Feng L, Shi X, Wang X, Yang Y, Yang K, Liu T, Yang G, Liu Z. Surface coating-dependent cytotoxicity and degradation of graphene derivatives: towards the design of non-toxic, degradable nano-graphene. Small. 2014; 10:1544–54. [PubMed: 24376215]
8. Kavitha T, Kang IK, Park SY. Poly(acrylic acid)-grafted graphene oxide as an intracellular protein carrier. Langmuir. 2014; 30:402–9. [PubMed: 24377671]
9. Yang K, Feng L, Hong H, Cai W, Liu Z. Preparation and functionalization of graphene nanocomposites for biomedical applications. Nat Protoc. 2013; 8:2392–403. [PubMed: 24202553]
10. Cheon YA, Bae JH, Chung BG. Reduced graphene oxide nanosheet for chemo-photothermal therapy. Langmuir. 2016; 32:2731–6. [PubMed: 26930106]
11. Wen H, Yin C, Du A, Deng L, He Y, He L. Folate conjugated PEG-chitosan/graphene oxide nanocomplexes as potential carriers for pH-triggered drug release. J Control Release. 2015; 213:e44–5.
12. Yang K, Wan J, Zhang S, Zhang Y, Lee ST, Liu Z. In vivo pharmacokinetics, long-term biodistribution, and toxicology of PEGylated graphene in mice. ACS Nano. 2011; 5:516–22. [PubMed: 21162527]
13. Chung AS, Lee J, Ferrara N. Targeting the tumour vasculature: insights from physiological angiogenesis. Nat Rev Cancer. 2010; 10:505–14. [PubMed: 20574450]

14. Hanahan D, Weinberg RA. Hallmarks of cancer: the next generation. Cell. 2011; 144:646–74. [PubMed: 21376230]
15. Hong H, Chen F, Zhang Y, Cai W. New radiotracers for imaging of vascular targets in angiogenesis-related diseases. Adv Drug Deliv Rev. 2014; 76:2–20. [PubMed: 25086372]
16. Radu A, Pichon C, Camparo P, Antoine M, Allory Y, Couvelard A, Fromont G, Hai MTV, Ghinea N. Expression of follicle-stimulating hormone receptor in tumor blood vessels. New Eng J Med. 2010; 363:1621–30. [PubMed: 20961245]
17. Siraj A, Desestret V, Antoine M, Fromont G, Huerre M, Sanson M, Camparo P, Pichon C, Planeix F, Gonin J. Expression of follicle-stimulating hormone receptor by the vascular endothelium in tumor metastases. BMC cancer. 2013; 13:246. [PubMed: 23688201]
18. Ferlin A, Pengo M, Selice R, Salmaso L, Garolla A, Foresta C. Analysis of single nucleotide polymorphisms of FSH receptor gene suggests association with testicular cancer susceptibility. Endocr Relat cancer. 2008; 15:429–37. [PubMed: 18430895]
19. Gartrell BA, Tsao C-k, Galsky MD. The follicle-stimulating hormone receptor: a novel target in genitourinary malignancies. Urol Oncol. 2013; 31:1403–7. [PubMed: 22513137]
20. Gloaguen P, Crépieux P, Heitzler D, Poupon A, Reiter E. Mapping the follicle-stimulating hormone-induced signaling networks. Front Endocrinol (Lausanne). 2011; 2:1–13. [PubMed: 22649356]
21. Keereweer S, Van Driel PB, Robinson DJ, Lowik CW. Shifting focus in optical image-guided cancer therapy. Mol Imaging Biol. 2014; 16:1–9. [PubMed: 24037176]
22. Xu Y, Pan D, Zhu C, Xu Q, Wang L, Chen F, Yang R, Luo S, Yang M, Yan Y. Pilot study of a novel ^{18}F-labeled FSHR probe for tumor imaging. Mol. Imaging Biol. 2014; 16:578–85.
23. Zhu C, Xu Q, Pan D, Xu Y, Liu P, Yang R, Wang L, Sun X, Luo S, Yang M. Prostate cancer imaging of FSHR antagonist modified with a hydrophilic linker. Contrast Media Mol Imaging. 2016; 11:99–105. [PubMed: 26286841]
24. Hong H, Yan Y, Shi S, Graves SA, Krasteva LK, Nickles RJ, Yang M, Cai W. PET of follicle-stimulating hormone receptor: broad applicability to cancer imaging. Mol Pharm. 2015; 12:403–10. [PubMed: 25581441]
25. Zhang XY, Chen J, Zheng YF, Gao XL, Kang Y, Liu JC, Cheng MJ, Sun H, Xu CJ. Follicle-stimulating hormone peptide can facilitate paclitaxel nanoparticles to target ovarian carcinoma in vivo. Cancer Res. 2009; 69:6506–14. [PubMed: 19638590]
26. Modi DA, Sunoqrot S, Bugno J, Lantvit DD, Hong S, Burdette JE. Targeting of follicle stimulating hormone peptide-conjugated dendrimers to ovarian cancer cells. Nanoscale. 2014; 6:2812–20. [PubMed: 24468839]
27. Fan L, Chen J, Zhang X, Liu Y, Xu C. Follicle-stimulating hormone polypeptide modified nanoparticle drug delivery system in the treatment of lymphatic metastasis during ovarian carcinoma therapy. Gynecol Oncol. 2014; 135:125–32. [PubMed: 25003656]
28. Mehlen P, Puisieux A. Metastasis: a question of life or death. Nat Rev Cancer. 2006; 6:449–58. [PubMed: 16723991]
29. Siegel RL, Miller KD, Jemal A. Cancer statistics, 2016. CA Cancer J Clin. 2016; 66:7–30. [PubMed: 26742998]
30. Cavnar SP, Rickelmann AD, Meguiar KF, Xiao A, Dosch J, Leung BM, Cai Lesher-Perez S, Chitta S, Luker KE, Takayama S, Luker GD. Modeling selective elimination of quiescent cancer cells from bone marrow. Neoplasia. 2015; 17:625–33. [PubMed: 26408255]
31. Hong H, Severin GW, Yang Y, Engle JW, Zhang Y, Barnhart TE, Liu G, Leigh BR, Nickles RJ, Cai W. Positron emission tomography imaging of CD105 expression with ^{89}Zr-Df-TRC105. Eur. J. Nucl. Med. Mol. imaging. 2012; 39:138–48.
32. Hong H, Zhang Y, Severin GW, Yang Y, Engle JW, Niu G, Nickles RJ, Chen X, Leigh BR, Barnhart TE, Cai W. Multimodality imaging of breast cancer experimental lung metastasis with bioluminescence and a monoclonal antibody dual-labeled with ^{89}Zr and IRDye 800CW. Mol. Pharm. 2012; 9:2339–49.
33. Chen F, Hong H, Shi S, Goel S, Valdovinos HF, Hernandez R, Theuer CP, Barnhart TE, Cai W. Engineering of hollow mesoporous silica nanoparticles for remarkably enhanced tumor active targeting efficacy. Sci Rep. 2014; 4:5080. [PubMed: 24875656]

34. Shi S, Yang K, Hong H, Chen F, Valdovinos HF, Goel S, Barnhart TE, Liu Z, Cai W. VEGFR targeting leads to significantly enhanced tumor uptake of nanographene oxide in vivo. Biomaterials. 2015; 39:39–46. [PubMed: 25477170]
35. Shi S, Yang K, Hong H, Valdovinos HF, Nayak TR, Zhang Y, Theuer CP, Barnhart TE, Liu Z, Cai W. Tumor vasculature targeting and imaging in living mice with reduced graphene oxide. Biomaterials. 2013; 34:3002–9. [PubMed: 23374706]
36. Chen F, Hong H, Zhang Y, Valdovinos HF, Shi S, Kwon GS, Theuer CP, Barnhart TE, Cai W. In vivo tumor targeting and image-guided drug delivery with antibody-conjugated, radiolabeled mesoporous silica nanoparticles. ACS Nano. 2013; 7:9027–39. [PubMed: 24083623]
37. Choi HS, Liu W, Misra P, Tanaka E, Zimmer JP, Ipe BI, Bawendi MG, Frangioni JV. Renal clearance of quantum dots. Nat Biotechnol. 2007; 25:1165–70. [PubMed: 17891134]
38. Zhang Y, Nayak TR, Hong H, Cai W. Graphene: a versatile nanoplatform for biomedical applications. Nanoscale. 2012; 4:3833–42. [PubMed: 22653227]
39. Francia G, Cruz-Munoz W, Man S, Xu P, Kerbel RS. Mouse models of advanced spontaneous metastasis for experimental therapeutics. Nat Rev Cancer. 2011; 11:135–41. [PubMed: 21258397]
40. Cassidy JW, Caldas C, Bruna A. Maintaining tumor heterogeneity in patient-derived tumor xenografts. Cancer Res. 2015; 75:2963–8. [PubMed: 26180079]
41. Maeda H, Nakamura H, Fang J. The EPR effect for macromolecular drug delivery to solid tumors: Improvement of tumor uptake, lowering of systemic toxicity, and distinct tumor imaging in vivo. Adv Drug Deliv Rev. 2013; 65:71–9. [PubMed: 23088862]
42. Chen XY, Chen WL, Ma M, Gu C, Xiao XR, Li B. The potential of follicle-stimulating hormone peptide-modified triptolide-loaded nanoparticles to induce a mouse model of premature ovarian insufficiency. Int J Nanomedicine. 2015; 10:2765–74. [PubMed: 25897221]
43. Snow-Lisy DC, Sabanegh ES Jr, Samplaski MK, Labhasetwar V. Anatomical Targeting Improves Delivery of Unconjugated Nanoparticles to the Testicle. J Urol. 2015; 194:1155–61. [PubMed: 25796115]
44. Olafsen T, Wu AM. Antibody vectors for imaging. Semin Nucl Med. 2010; 40:167–81. [PubMed: 20350626]
45. Kaur S, Venktaraman G, Jain M, Senapati S, Garg PK, Batra SK. Recent trends in antibody-based oncologic imaging. Cancer Lett. 2012; 315:97–111. [PubMed: 22104729]
46. Hong H, Zhang Y, Orbay H, Valdovinos HF, Nayak TR, Bean J, Theuer CP, Barnhart TE, Cai W. Positron emission tomography imaging of tumor angiogenesis with a $^{61/64}$Cu-labeled F(ab′)$_2$ antibody fragment. Mol. Pharm. 2013; 10:709–16.
47. Jhaveri A, Deshpande P, Torchilin V. Stimuli-sensitive nanopreparations for combination cancer therapy. J Control Release. 2014; 190:352–70. [PubMed: 24818767]
48. Liu Y, Rohrs J, Wang P. Advances and challenges in the use of nanoparticles to optimize PK/PD interactions of combined anti-cancer therapies. Curr Drug Metab. 2014; 15:818–28. [PubMed: 25705903]
49. Yu HN, Richardson TE, Nataraja S, Fischer DJ, Sriraman V, Jiang X, Bharathi P, Foglesong RJ, Haxell TF, Heasley BH, Jenks M, Li J, Dugas MS, Collis R, Tian H, Palmer S, Goutopoulos A. Discovery of substituted benzamides as follicle stimulating hormone receptor allosteric modulators. Bioorg Med Chem Lett. 2014; 24:2168–72. [PubMed: 24685543]
50. Chen D, Dougherty CA, Zhu K, Hong H. Theranostic applications of carbon nanomaterials in cancer: Focus on imaging and cargo delivery. J Control Release. 2015; 210:230–45. [PubMed: 25910580]

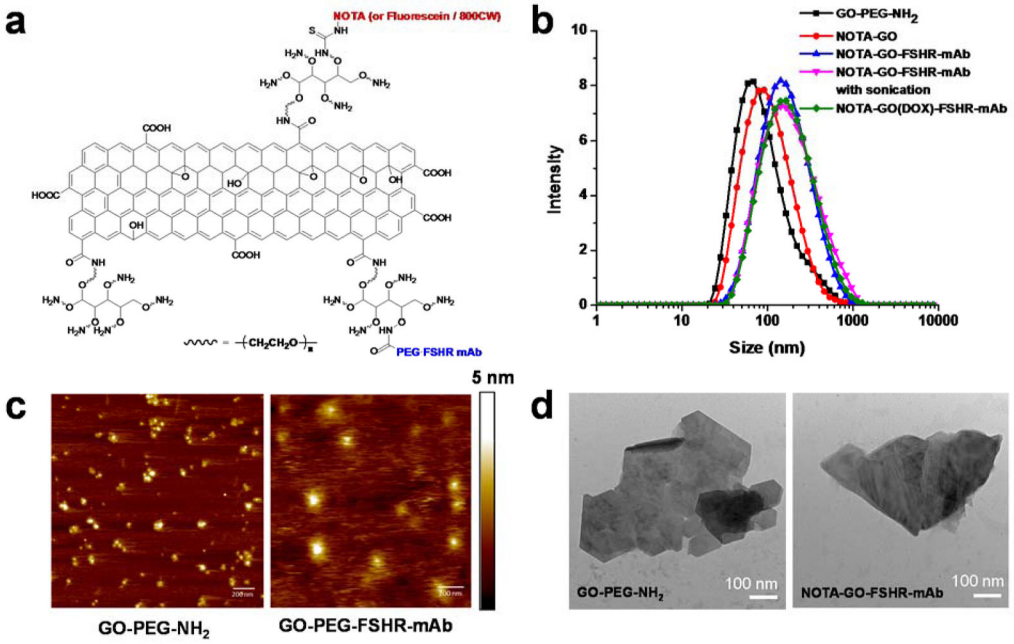

Figure 1.

Schematic structural information (a), dynamic laser scattering (DLS) measurements (b), atomic force microscopy (AFM) images (c), and transmission electron microscopy (TEM) images (d) of nano-graphene conjugates.

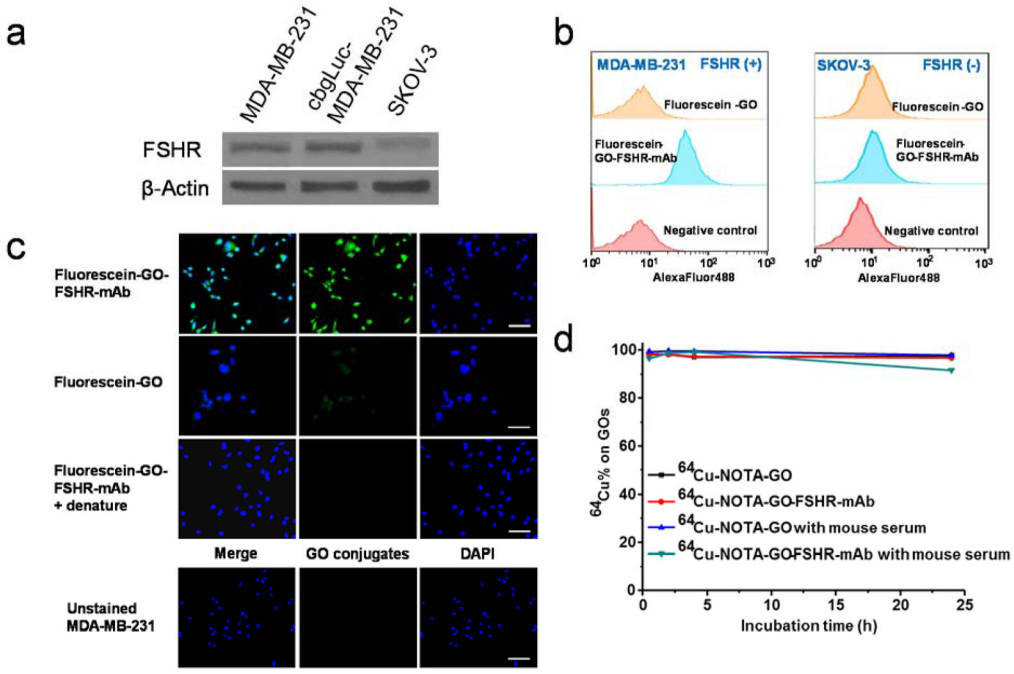

Figure 2.

In vitro characterization of the GO conjugates. (a) Western blotting of FSHR and β-actin in MDA-MB-231, cbgLuc-MDA-MB-231, and SKOV-3 cells. No observable change of FSHR was witnessed in MDA-MB-231 post transfection of cbgLuc. (b) Flow cytometry analysis of the GO conjugates in FSHR-positive MDA-MB-231 cells and FSHR-negative SKOV-3 cells. (c) Representative confocal fluorescence images of in MDA-MB-231 cells stained with fluorescein-GO-FSHR-mAb, fluorescein-GO and sonication-denatured fluorescein-GO-FSHR-mAb. Blank MDA-MB-231 cells were also used as a control. Scale bar: 50 μm. (d) Serum stability test of ^{64}Cu-labeled GO conjugates after incubation in complete mouse serum for 24 h.

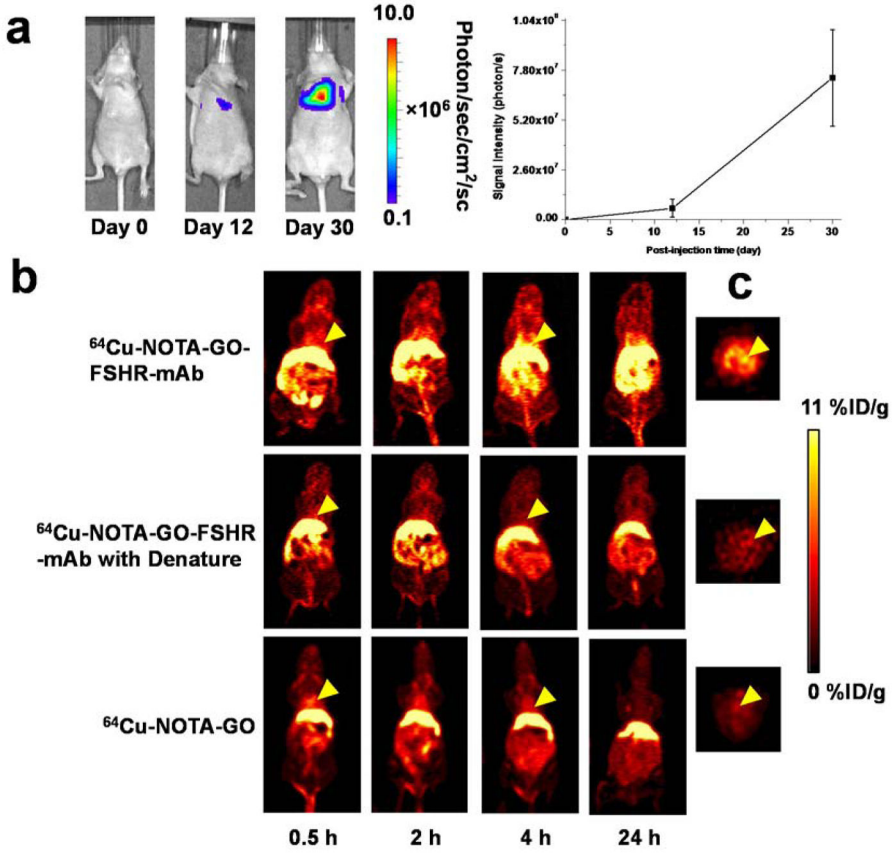

Figure 3.

Experimental murine model of breast cancer lung metastasis and *in vivo* PET imaging with ^{64}Cu-labeled GO conjugates. (a) Serial bioluminescence images and BLI signal intensity from the thoracic area of mice after intravenous injection of cbgLuc-MDA-MB-231 cells; (b) Serial coronal PET imaging of cbgLuc-MDA-MB-231 tumor-bearing mice at different time points post-injection of ^{64}Cu-NOTA-GO-FSHR-mAb, ^{64}Cu-NOTA-GO-FSHR-mAb with denature and ^{64}Cu-NOTA-GO; (c) The cross-sectional slices of mice containing cbgLuc-MDA-MB-231 tumor nodules at 4 h post-injection of ^{64}Cu-NOTA-GO-FSHR-mAb, ^{64}Cu-NOTA-GO-FSHR-mAb with denature and ^{64}Cu-NOTA-GO.

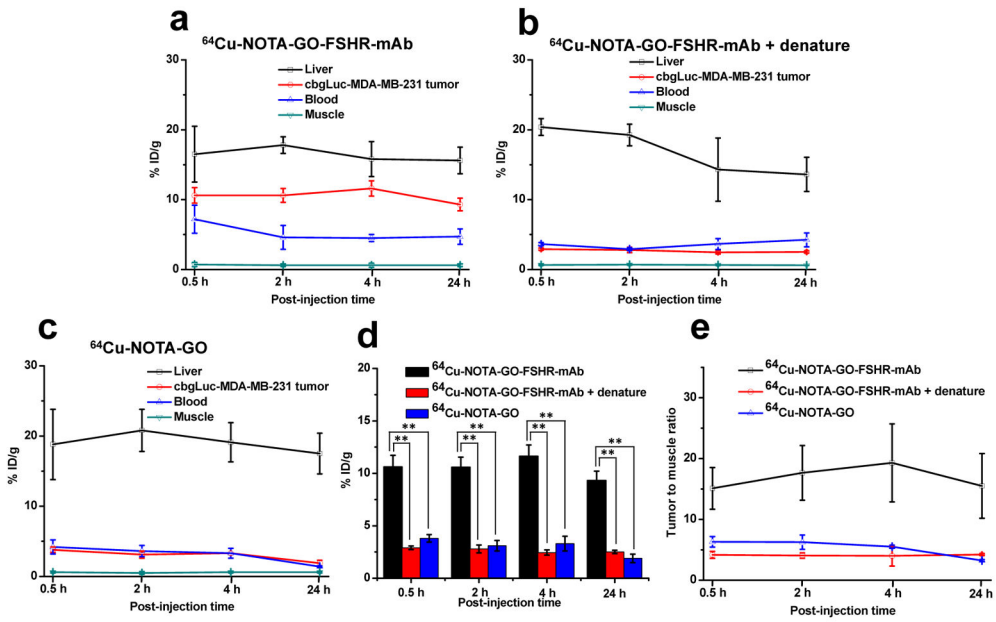

Figure 4.

Quantitative region-of-interest (ROI) analysis of PET. (a) Time activity curves of blood, liver, tumor and muscle upon intravenous injection of ^{64}Cu-NOTA-GO-FSHR-mAb. (b) Time activity curves of blood, liver, tumor and muscle upon intravenous injection of ^{64}Cu-NOTA-GO-FSHR-mAb post sonication denature. (c) Time activity curves of blood, liver, tumor and muscle upon intravenous injection of ^{64}Cu-NOTA-GO. (d) Comparison of the uptake in cbgLuc-MDA-MB-231 tumor nodules from these three groups. **, P<0.01. (e) Tumor-to-muscle (T/M) ratios from these three groups.

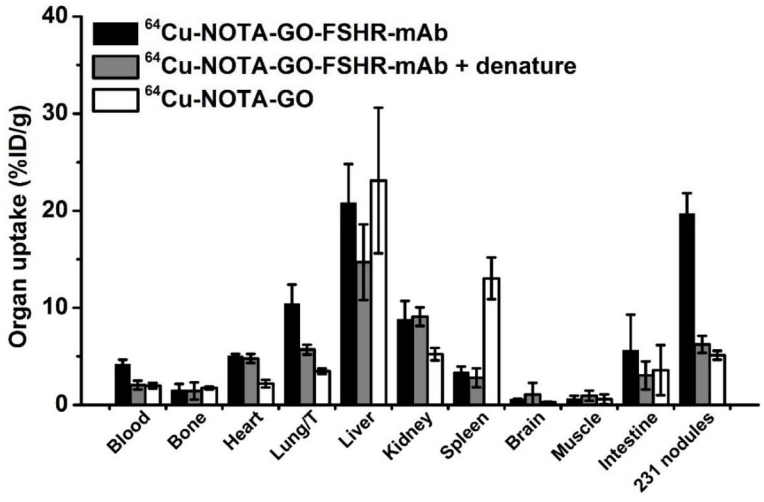

Figure 5.

Ex vivo biodistribution in mice at 24 h post-injection of ^{64}Cu-labeled GO conjugates. Some of the tumor nodules (n = 5 per group) inside the lungs were also separated for radioactivity measurement.

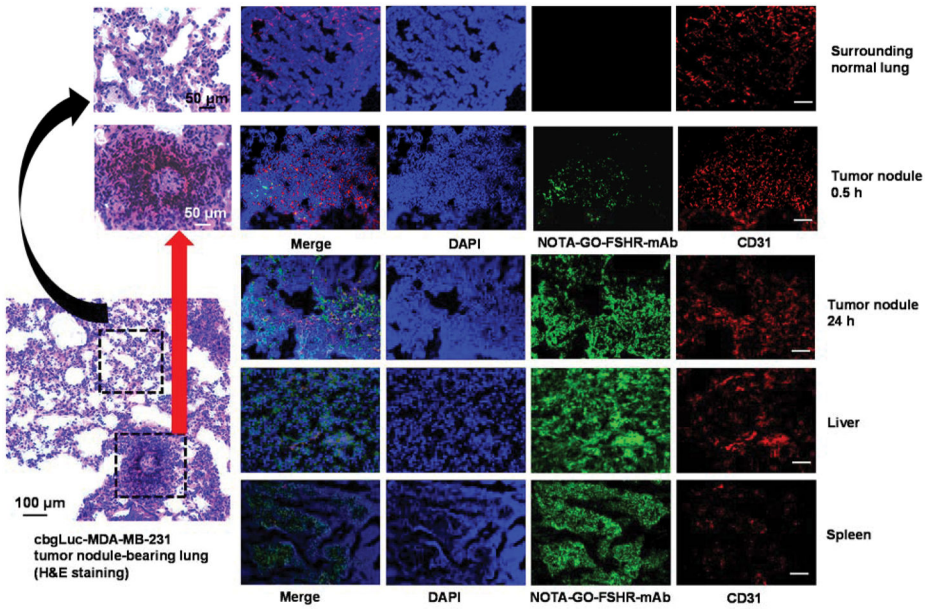

Figure 6.

Immunofluorescence staining of primary tissues (tumor nodules-containing lungs, liver, and spleen). Cell nuclei were visualized by DAPI (blue), CD31 was detected with an anti-mouse CD31 antibody (red), and NOTA-GO-FSHR-mAb was visualized by a secondary rat-anti-mouse IgG (green, FSHR-mAb within NOTA-GO-FSHR-mAb serves as the primary antibody). H&E staining was carried out in tumor nodules-containing lungs to discriminate tumor nodules from normal surrounding tissues. Magnification: 200×. Scale bar: 100 μm.

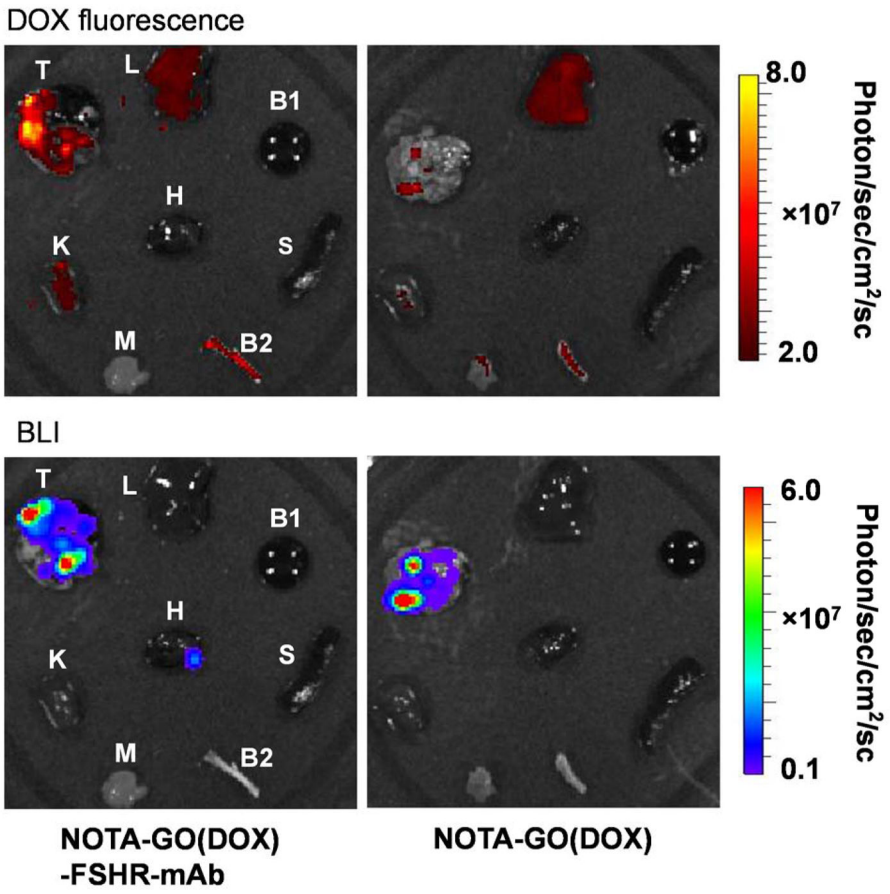

Figure 7.

In vivo enhanced drug delivery via GO conjugates. *Ex vivo* fluorescence images of DOX (the model drug) in the major organs/tissues at 30 min after intravenous injection of NOTA-GO(DOX)-FSHR-mAb and NOTA-GO(DOX) were shown in the upper panels. BLI images of same major organs/tissues were shown in the lower panels to confirm the location(s) of the tumor nodules. T, cbgLuc-MDA-MB-231 tumor nodules-bearing lung; L, liver; K, Kidney; H, heart; S, spleen; M, muscle; B1, blood; B2, bone.

Table 1

The ROI analysis of major organs from PET (unit: %ID/g)

Time Point	Tissue	^{64}Cu-NOTA-GO-FSHR-mAb	^{64}Cu-NOTA-GO-FSHR-mAb with denature	^{64}Cu-NOTA-GO
0.5 h	Liver	16.5 ±4.0	20.4 ±1.2	18.8 ±5.0
	Tumor	10.6 ±1.1	2.9 ±0.2	3.8 ±0.4
	Blood	7.2 ±2.0	3.6 ±0.2	4.2 ±1.0
	Muscle	0.7 ±0.3	0.7 ±0.1	0.6 ±0.1
2 h	Liver	17.8± 1.2	19.3 ±1.5	20.8 ±3.0
	Tumor	10.6 ±1.0	2.8 ±0.4	3.1 ±0.5
	Blood	4.6 ±1.7	2.9 ±0.2	3.6 ±0.8
	Muscle	0.6 ±0.2	0.7 ±0.1	0.5 ±0.2
4 h	Liver	15.8± 2.5	14.3 ±4.5	19.1 ±2.8
	Tumor	11.6± 1.1	2.4 ±0.2	3.3 ±0.7
	Blood	4.5 ±0.5	3.6 ±0.8	3.3 ±0.7
	Muscle	0.6± 0.3	0.6 ±0.1	0.6 ±0.2
24 h	Liver	15.6± 1.9	13.6 ±2.5	17.5 ±2.9
	Tumor	9.3 ±0.9	2.5 ±0.2	1.9 ±0.4
	Blood	4.7± 1.1	4.2 ±1.0	1.4 ±0.1
	Muscle	0.6 ±0.2	0.6 ±0.02	0.6 ±0.1

Table 2

the tumor-to-muscle (T/M) ratios of different organs at different time points

Time Point	^{64}Cu-NOTA-GO-FSHR-mAb	^{64}Cu-NOTA-GO-FSHR-mAb with denature	^{64}Cu-NOTA-GO
0.5 h	15.1±3.4	4.2±0.6	6.3±0.9
2 h	17.6±4.5	4.1±0.4	6.2±1.2
4 h	19.3±6.4	4.0±1.6	5.5±0.3
24 h	15.5±5.3	4.2±0.2	3.2±0.2